SUBSTRATE EFFECTS FROM FORCE CHAIN DYNAMICS IN DENSE GRANULAR FLOWS

A Thesis
Presented to
The Academic Faculty

By

Joseph J. Estep

In Partial Fulfillment
Of the Requirements for the Degree
Master of Science in Earth and Atmospheric Sciences

Georgia Institute of Technology

May 2011

SUBSTRATE EFFECTS FROM FORCE CHAIN DYNAMICS
IN DENSE GRANULAR FLOWS

Approved By:

Dr. Josef Dufek
School of Earth and Atmospheric Sciences
Georgia Institute of Technology

Dr. Kurt Frankel
School of Earth and Atmospheric Sciences
Georgia Institute of Technology

Dr. Andrew Newman
School of Earth and Atmospheric Sciences
Georgia Institute of Technology

Date Approved: March 28, 2011

ACKNOWLEDGEMENTS

I want to thank my advisor, Dr. Josef Dufek, for the incredible opportunity to work under his supervision as a graduate assistant. His insightful conversations, invaluable advice, constructive feedback, continual patience, and tremendous support were vital for the success of this work. My gratitude also goes to Dr. Andrew Newman and Dr. Kurt Frankel, who also provided helpful insight and feedback during this process. I appreciate the positive support of my fellow graduate students and Geophysics faculty, and the useful perspectives they provided during the development of my research. I would like to acknowledge Janet Patterson of Duke University's Machine Shop for help with experimental material production. Finally, I want to thank my family and friends for their endless patience and encouragement.

TABLE OF CONTENTS

ACKNOWLEDGMENTS iii

LIST OF TABLES v

LIST OF FIGURES vi

SUMMARY vii

CHAPTER 1. INTRODUCTION 1

CHAPTER 2. EXPERIMENTAL TECHNIQUES 4

2.1 Materials 6

2.2 Experimental Methods 7

2.3 Calibration 9

2.4 Image Processing 12

CHAPTER 3. RESULTS 13

CHAPTER 4. DISCUSSION 19

4.1 Conclusion 24

REFERENCES 25

LIST OF TABLES

Table 1 Comparison between applied force values and equitable disk number by weight in terms of calibration fringe threshold values 12

Table 2 Dimensional measured values for flow deposits. *The available run-out distance beyond inclination was 0.30 meters; therefore this represents a minimum value 13

LIST OF FIGURES

Figure 1 (A & B) An example of a stress pattern observed on a single photoelastic disc within a force chain, where the white triangles indicate the points of applied stress 5

Figure 2 A schematic diagram of the plane polariscope setup used for our photoelastic experimentation 5

Figure 3 Snapshot of experimental flow illustrated with inclined *x–z* coordinate system and shear velocity (*u*) diagram 6

Figure 4 (A & B) Schematic view of the calibration setup used during our experimentation.....11

Figure 5 (A & B) Sample image illustrated to show where localized and averaged forces are derived. B. Eulerian temporal regressions describe cumulative bed force magnitudes 14

Figure 6 Localized bed force magnitudes from force chains compared to averaged bed force magnitudes calculated from flow body height for rigid and erodible cases 15

Figure 7 Extent of force propagation into erodible bed section correlated to magnitude of bed force at chain-bed contact point for each ramp inclination 16

Figure 8. Pictured above are images of the erodible bed section, which show force propagation into the bed section and ahead of the flow front.....17

Figure 9 (A & B) Temporal regressions average length, total length, and number of force chains for each incline from rigid bed experiments 18

SUMMARY

Granular materials are composed of solid, discrete particles and exhibit mechanical behavior that differs from those of fluids and solids. The rheology of granular flows is principal to a suite of natural hazards. Laboratory experiments and numerical models have adequately reproduced several features observed in terrestrial gravity driven geophysical flows; however, quantitative comparison to field observations exposes a failure to explain the high mobility and duration of many of these flows. The ability of a granular material to resist deformation is a function of the force chain network inherent to the material. This investigation addresses the evolutionary character of force chains in unconfined, two-dimensional, gravity driven granular flows. Our particular emphasis concerns the effects of stress localization on the substrate by dynamic force chain evolution and the implications for bed erosion in dense granular flows. Experimental systems employing photoelastic techniques provide an avenue for quantitative force analysis via image processing and provide dataset that can be used validate discrete element modeling approaches. We show that force chains cause extreme bed force localization throughout dynamic granular systems in spatial and temporal space; and that these localized forces can propagate extensively into the substrate, even ahead of the flow front.

CHAPTER 1. INTRODUCTION

Granular materials are composed of solid, discrete particles that dissipate energy when the constitutive particles interact – for example, through friction (Behringer et. al. 2008). The physical characteristics of granular materials exhibit mechanical properties that differ from those of solids and liquids. For instance, granular flows often include non-elastic materials and can show nonlinear dependence for shear stresses, thus exhibiting non-Newtonian behavior. Rheology of granular materials is principal to a suite of geophysical processes (Furbish et. al. 2008); including dry ravel, sand dune migration, as well as the motion of landslides, debris flows, pyroclastic flows, avalanches, and fault systems. These events are relevant to civil engineering, geophysics and physics (Majmudar et. al. 2005). Gravity driven granular flows are principal components in landscape evolution of the Earth and other planets; and produce natural hazards that threaten populations and infrastructure. Increased climate instability and landscape use may boost the frequency and impact of geophysical flows, such as debris flows (Iverson, 2011).

Numerical models and laboratory experiments of granular flows have successfully reproduced several features observed in terrestrial gravity driven geophysical flows. When compared quantitatively to field observations, however, empirical and numerical data fails to explain the high mobility of these flows that can travel long distances even on modest slopes (Mangeney et. al. 2007). Inter-particle forces in granular materials often form a distributive network of force chains (or stress chains) as opposed to being uniformly distributed (Majmudar et. al. 2005). The ability of a granular material to resist deformation is a function of the force chain network inherent to the media. The responses of these force chain networks to applied

stresses ultimately define the material's macroscopic character. Previous research (Furbish et al., 2008) shows that flow motion in these systems involves the continuous buildup and collapse of granular force chains. The works of Furbish et. al. (2008) introduce statements of conservation (1) and force balance (2) which describe the production and destruction of force chains in a dynamic shearing granular system with motion driven by acoustic vibrations.

$$\frac{dN}{dt} = P - Q_\gamma - Q_f - Q_T \quad (1)$$

$$\tau = \frac{F}{B} \sim k\delta \frac{\alpha\gamma}{\alpha_\gamma \gamma + \beta f + \varepsilon} \sim k\delta N \quad (2)$$

In equation (1) N represents the number of force chains per unit area, P denotes force chain production, while Q_γ, Q_f, and Q_t are force chain destruction by shearing, vibrations, and collisions, respectively. The force balance in equation (2) describes stress τ in terms of the force F over an area B, where k is grain-contact stiffness, α is a factor related to the shear rate γ, α_γ describes 'aging' of chains during rotation as their stability gives way to destruction, β is the proportion of chain disruptions per unit time, and ε is the reciprocal of mean free time for grain motion. In this formulation the force chains are conserved through destruction by vibrations, shear, and collisions balanced by production via shear. We will examine how this theoretical framework and our empirical investigation relate later in the discussion. Understanding force chains as a function of their temporal and spatial correlations, particularly in response to forces at system boundaries is a rudimentary goal of granular mechanics.

Several mechanisms have been proposed to explain the high mobility of gravitational flows, such as: upward air currents, basal 'hovercraft' action, rock melting, acoustic and fine dust induced fluidization, frictional heat, particle communition, polydiversity, and water or air

contained within the flow (Furbish et. al. 2008, Mangeney et. al. 2007). Alternatively, the erosion of material already in place on the underlying solid topography is proposed to significantly impact the mobility of granular flows and the dynamics of flow transportation (Mangeney et. al. 2007). The entrainment of the substrate by the flowing mass could potentially increase or decrease flow mobility depending on flow dynamics and the physical character of the substrate (Iverson, 1997).

Stress localizations via force chains have been well documented for confined, static and shearing granular systems. The primary questions we want to address with this work are as follows: (1) Do the stress localizations characteristic of confined granular systems translate to unconfined dynamic systems, and – if so – are they important for bed stresses on the substrate of unconfined gravity driven granular flows? (2) Do the effects from force chains in unconfined gravity driven granular flows carry significant implications for erosion and entrainment of the substrate?

CHAPTER 2. EXPERIMENTAL TECHNIQUES

Transparent materials, such as glass or certain polymers, become birefringent when stressed. When viewed in a field of circularly or plane polarized light, one can observe the transmission of the internal stresses caused by forces acting on the material boundaries (Majmudar et. al. 2005). This property has been used in the past extensively; primarily in structural engineering models, to observe elastic stress distributions in small-scale models of structures in polarized light, e.g., dams, bridges, and mechanical components (Behringer et. al. 2008). The same technique can be used to observe the force chains within a sample of a granular material made of transparent particles. This photoelastic technique provides an avenue for quantitative analysis of the force chain networks, because the intensity of transmitted light is proportional to the inherent stresses (Figure 1; Behringer et. al. 2008, Majmudar et. al. 2005). Figure 2 shows a schematic of the light/lens setup used for our photoelastic experimentation, and Figure 3 illustrates the shearing motion of the 2D flows and provides a snapshot image of a transient force chain network. Shearing and compression experiments conducted by Behringer (2008) and Majmudar (2005) indicate mesoscale force distribution through stress propagation in filamentary force chain networks, in which a fraction of the total number of particles carries the majority of the force (Geng, 2003).

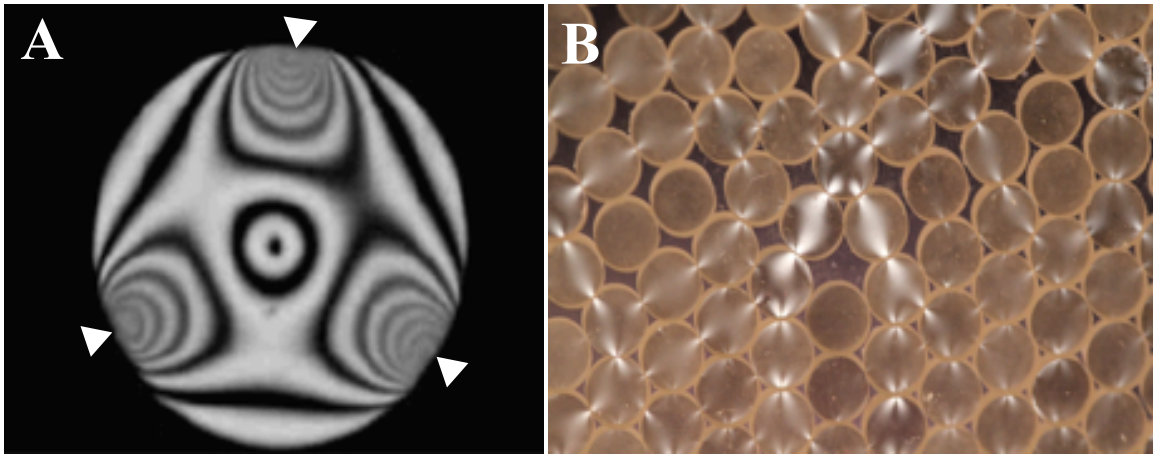

Figure 1. (a) An example of a stress pattern observed on a single photoelastic disc within a force chain, where the white triangles indicate the points of applied stress. The lighter filamentary shapes on the disk are fringes, which indicate the magnitude of strain experienced by the disk – ergo, the fringe pattern can provide an avenue to quantify applied force. Modified from Majmudar et. al. 2005. (b) An image from one of our experiments of the stressed photoelastic granular material exhibiting force chains. Notice that the fringe order for the disks pictured here does not exceed one, which is a characteristic that continued for the duration of our experimentation.

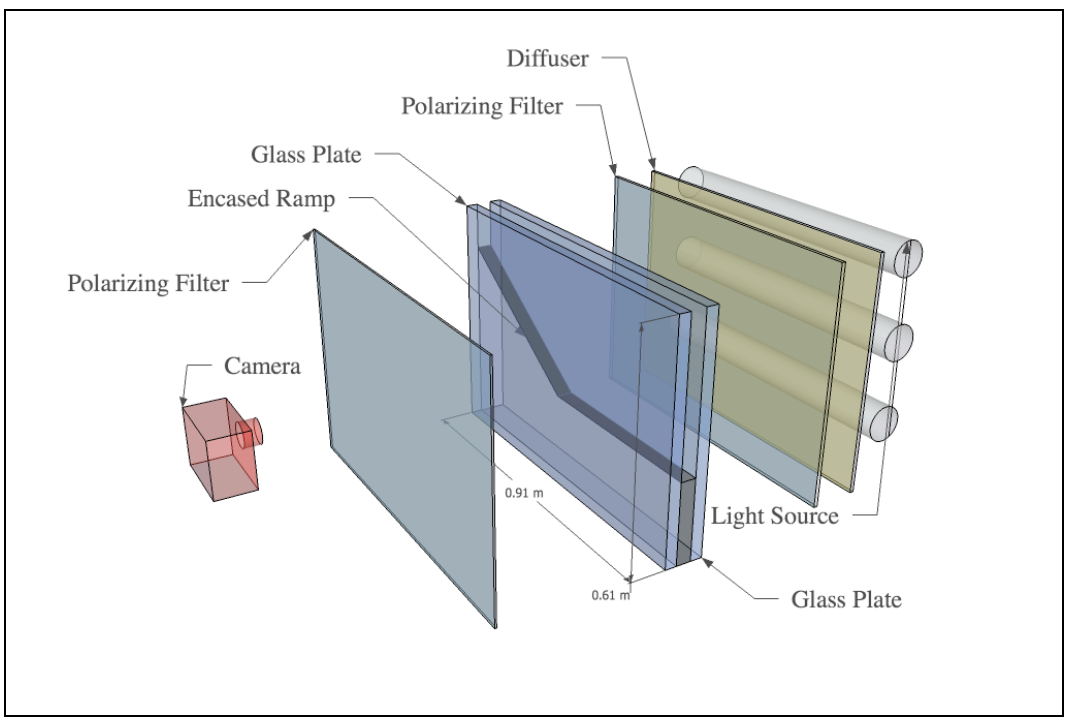

Figure 2. A schematic diagram of the plane polariscope setup used for our photoelastic experimentation. Images depicted here are not drawn to scale.

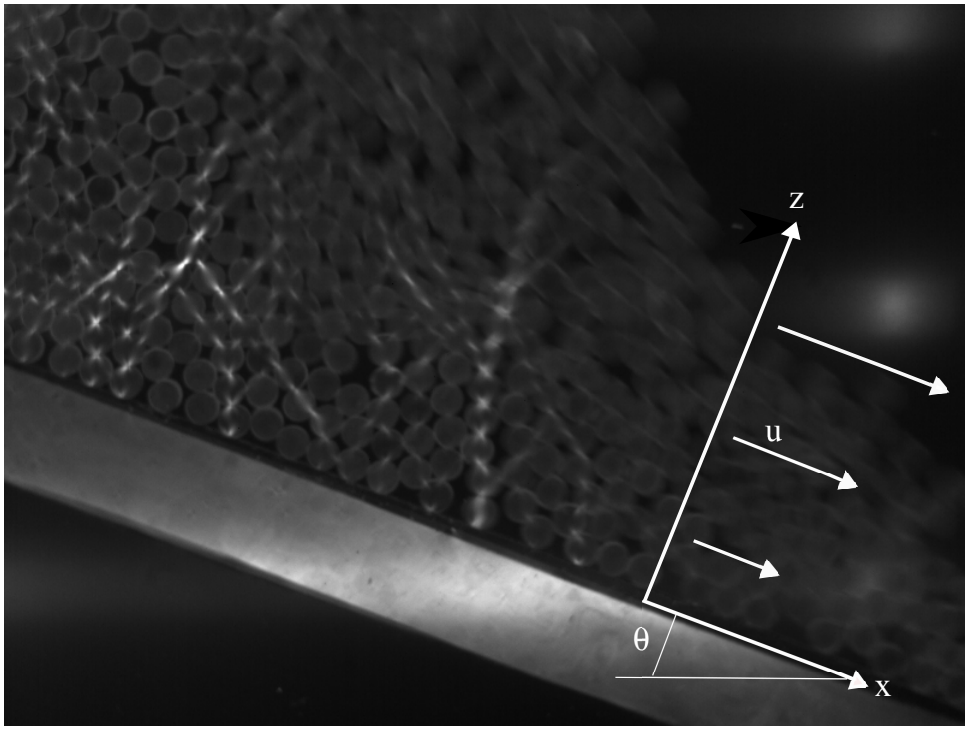

Figure 3. Snapshot of experimental flow illustrated with inclined *x–z* coordinate system and shear velocity (*u*) diagram. The optical activity of the photoelastic disks makes primary force-chain participants, secondary participants, and spectators easily identifiable.

2.1 Materials

To utilize the photoelastic technique and implement it into our work, we first constructed an apparatus to house the material constituting our granular media. Internal structuring for the apparatus, including: the release gate, ramp, run-out bed, erodible bed section, retaining wall, and spacers; was formed from 3.18 x 10^{-3} m thickness cell cast clear Plexiglass sheets, and 7.62 x 10^{-5} m thickness Dupont clear polyester film sheets. Clear glass panes measuring 0.91 m x 0.61 m x 2.38 x 10^{-3} m housed the acrylic internals. Retention hoppers, used for delivery and removal of the granular media from the apparatus, were also constructed from the Plexiglass material. Two ramp configurations were employed during the experimentation: rigid and erodible. The rigid configuration was a straight, rigid bed positioned at a desired inclination relative to level. The erodible configuration was similar to the rigid, but included a 0.12 m long x 0.04 m deep

rectangular section cut out of the bed, initiated 0.43 m from the high end of the ramp. Granular media occupied this cutout area to replicate erodible substrate conditions.

The granular media we chose for our experiments consisted of 0.006 m diameter, 1180 kg/m^3 density disks made from Vishay Precision Group's PSM-4 PhotoStress model material. Because of its low-modulus and constant sensitivity character, this material was deemed the best available for our purposes. The disks were lightly coated with flour to minimize inter-disk adhesion, and from 2100 to 2400 were used during each individual experimental run.

We constructed the plane polariscope necessary to visualize force chains present in the granular media. Three 0.36 m fluorescent lights were mounted horizontally in parallel arrangement with 0.08 m vertical spacing, and placed 0.4 m behind the back glass pane of the apparatus. In between the apparatus and the lights were placed a 0.28 m x 0.46 m Rosco Laboratories linear polarizing film and equally dimensioned diffuser sheet, respectively. On the face of the front glass plane of the apparatus was a second polarizing, oriented with orthogonal polarity relative to the larger backside polarizing film. Each of the polarizing film and diffuser sheet facial positions were adjusted to frame the area of interest for individual experimental runs. The experimental activity was recorded at 200 fps by a Miro Phantom high-speed camera, equipped with a Pentax CCTV 50 mm lens, and positioned 0.55 m from the front glass pane of the apparatus (opposite the lighting arrangement).

2.2 Experimental Methods

A suite of experiments, consisting of 24 individual flows, was conducted during our work. Three ramp inclinations, 10, 20, and 30 degrees, were employed for both the rigid and erodible bed sections. In the rigid bed case we used two focus areas, the first of which was

positioned centering the release gate at the initiation point of the flows. The second focus area was located down slope, and centered 0.185 m before the terminal end of the apparatus. Four flows were initiated at each inclination (two per focus area), and upon cessation the following were measured and recorded: run-out distance at the terminus, evacuated distance from initiation point, and jamming height at the head and toe of flow deposit. The high-speed imagery captured during these runs provided a means to record the following: flow duration, bed forces, chain counts, chain lengths, chain frequency, fringe orders, and spatial characteristics. In the erodible bed case we also used two focus areas; the first was the same as for the rigid inquires, and the second framed the erodible bed section down-slope from the release gate. Four flows were also processed at each inclination for the erodible bed case, two for each focus area. Supplemental data of force propagation distance and magnitude into the bed material was gathered for the erodible bed experiments.

Preparation for the flows initiated with delivery of the granular media into the apparatus via a retention hopper. The hopper was attached to the top of the apparatus, and the particles were released into the vacant upper portion of the housing. In this way the particles self-aligned into a random arrangement, and formed a static granular system due to confinement by the release gate. Once in place, the disk arrangement was recorded, and the retention hopper placed at the terminal end of the apparatus for disk retrieval. Flow motion was initiated by the removal of the release gate, which allowed the collapse of the static disk structure; resulting in an unconfined, gravity driven, dense granular flow moving down slope within the apparatus. Video recording captured the event, and upon cessation the deposit still image was also recorded.

2.3 Calibration

In order to accurately quantify the force magnitudes carried within the observed stress chains, a proper calibration of the stress – strain relationship is necessary. Conventional low-modulus PhotoStress calibration is achieved by the imposed-curvature method (Vishay, 2010). For most PhotoStress coated surfaces, the traditional approach to photoelastic calibration is to impose a series of known strains on simply shaped (typically a beam or rod) material with photoelastic coating, record the applied stress and resultant fringing, and use this information to quantify the strain and/or stress to the more complex structure under investigation. Multiplicative fringing (a fringe order greater than one) indicates rather large stresses relative to the modulus of the photoelastic material. For a fringe order less than one, the affected, or optically active, area of the photoelastic material increases with an increase in strain. However, when the fringe order exceeds one, the region of birefringence no longer requires growth. Instead, the fringe pattern may gain complexity within the same area. This is especially true then the optically active area considered is the entirety of material being investigated.

Our experimental granular systems possess unique characteristics, which allow us to justify an alternative calibration technique for our work. Most importantly, the small forces relative to common photoelastic applications result in a restrictive nature on the magnitude of fringing in our experiments, which never exceed an order of one. This is due to the small size and density of the disks, and the small scale of the granular systems employed. The discrete monodisperse character of the disks, along with the limited fringing observed means that the area of optical activity on a given unit is proportional to the force imposed on the boundaries of the unit. We use this relationship as the proxy for an incremental calibration scheme that correlates contact forces with area of optical activity.

Four threshold fringe magnitudes that encompassed the spectrum observed during the experiments were established and systematically reproduced: zero – no visible fringing, contact (or quarter) – fringe initiation at contact point on disk boundary, half – fringe propagation reaches midway through disk, full – fringe propagation covers the full diameter of the disk. Figure 4A shows a schematic diagram of the calibration setup. A 2D hopper, used as an alignment guide for the disks, was suspended 0.003 m above the surface of a digital scale. Four disks were placed on the scale in a double layer arrangement, and their cumulative weight recorded; this constitutes the 'zero fringe' case. The double layer allows for clear visibility of fringing, which is necessary for imaging and accurate reproduction of fringe magnitudes. A dSLR camera was used to image the calibration sequences. A manually controlled acrylic arm applied stress to the upper disk until the appropriate amount of fringing was produced, and the scale weight reading was recorded. This method was repeated for each of the threshold fringe magnitudes, ten times each. The scales weight readings were converted to force units that were normalized for an individual disk experiencing stress applied at one point of contact. Subtracting the residual self-applied forcing from the disks own weight was the final refinement of the calibration data. Figure 4B shows the results of our calibration procedure. The calibration data, although discrete to threshold values, encompasses the magnitudes of fringing observed throughout the suite of conducted experiments. Because of this fringe containment and relatively small optically active area available between threshold fringe levels, a simple linear interpolation between calibration data points is reasonable. Further justification for the interpolation lies in the fact that members of prominent force chains show fringe orders between the half and full fringe calibration values. We define a quantity, the fringe factor, that is the fractional area of a disk that is optically active; thus if a disk has a fringe factor of 0.5, then half of its facial area is

optically active. Table 1 compares calibration fringe thresholds to the number of disks whose combined weight would create a force equitable to the force applied to create each fringe threshold.

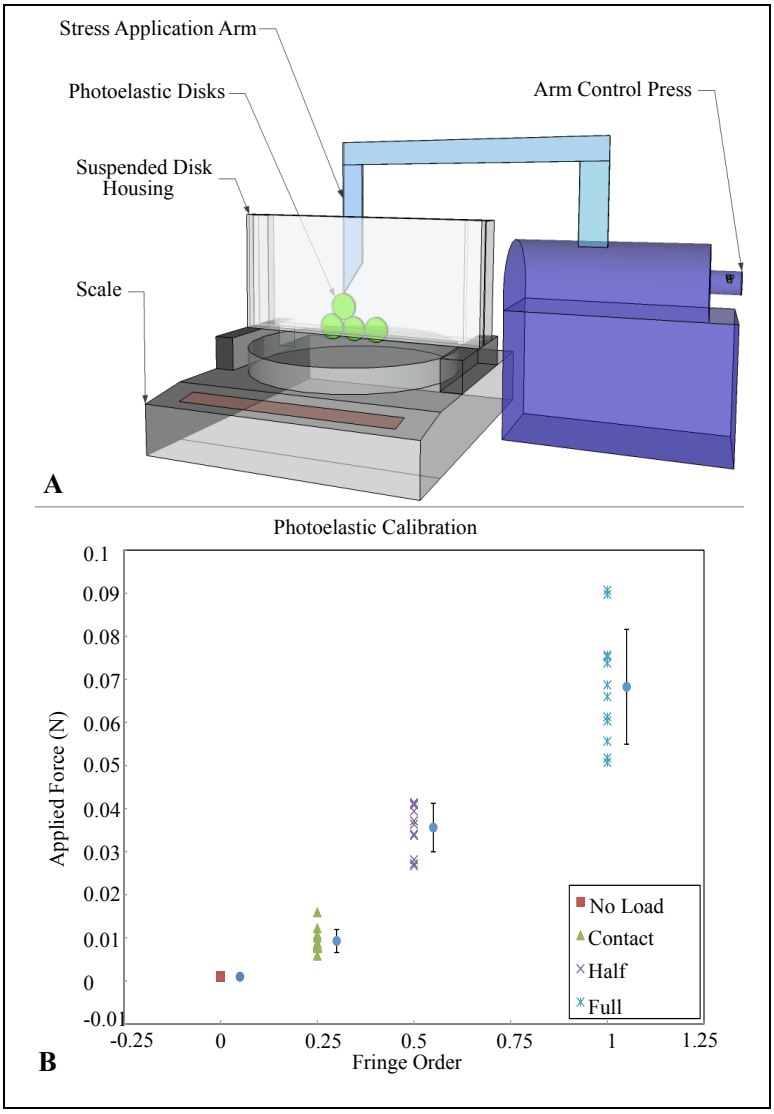

Figure 4. A. Schematic view of the calibration setup used during our experimentation. An acrylic arm applies stress to a photoelastic disk until the desired fringe magnitude is reached. The underlying digital scale records the weight change; which is used to calculate the applied force. B. Plot shows the calibration results in terms of fringe threshold values. Since the fringing observed during experimentation falls within the bounds of our calibration data, interpolation between the discrete threshold values is justifiable. Note that the mean data points and deviation bars are offset so they are distinguishable from standard data.

Table 1. Comparison between applied force values and equitable disk number by weight in terms of calibration fringe threshold values.

Fringe Threshold	Number of disks to equal applied force	Force applied during calibration in Newtons
None	1	0.001
Contact	9.55	0.009
Half	36.68	0.036
Full	70.34	0.068

2.4 Image Processing

Information from the calibration sequence images was implemented into an image-processing algorithm, which was written using MATLAB to extract data from the experiments. Individual frames from the video clips of each run were parsed into sequential tiff images. The image sequences were processed through the program; which identified the force chain fringe patterns and converted them into binary form, filtered the magnitudes by fringe thresholds, and computed several parameter values for the selected force chains. The program saved output files containing force chain counts, average and total lengths, and relative magnitudes.

CHAPTER 3. RESULTS

Flow durations for each incline, recorded as the time elapsed between flow initiation and the establishment of a static deposit, were as follows: 10º, 1.74 ± 0.16 s; 20º, 2.18 ± 0.13 s; and 30º, 2.62 ± 0.21 s. Table 2 displays the measured dimensional flow deposit values for several parameters. Run-out distance was the horizontal distance the flow reached beyond the inclined ramp. Evacuated length refers to the down-slope distance between the flow deposit and the retaining wall at the top of the flow initiation point. Jamming height at the head and toe describes the height of the flow deposit at the retaining wall located above the flow initiation point and the terminal end of the retention hopper, respectively.

Table 2. Dimensional measured values for flow deposits. *The available run-out distance beyond inclination was 0.30 meters; therefore this represents a minimum value.

Rigid			
Incline	10º	20º	30º
Run-out Distance (m)	0.041 ± 0.028	0.162 ± 0.026	0.300 ± 0.000*
Evacuated Length (m)	0.000 ± 0.000	0.000 ± 0.000	0.056 ± 0.028
Jamming Height @ Head (m)	0.186 ± 0.002	0.099 ± 0.003	0.000 ± 0.000
Jamming Height @ Toe (m)	0.000 ± 0.000	0.000 ± 0.000	0.009 ± 0.003
Erodible			
Incline	10º	20º	30º
Run-out Distance (m)	0.069 ± 0.029	0.153 ± 0.010	0.278 ± 0.021
Evacuated Length (m)	0.000 ± 0.000	0.000 ± 0.000	0.014 ± 0.022
Jamming Height @ Head (m)	0.187 ± 0.012	0.130 ± 0.002	0.005 ± 0.001
Jamming Height @ Toe (m)	0.000 ± 0.000	0.000 ± 0.000	0.002 ± 0.003

Figure 5 presents Eulerian temporal regressions of total bed force magnitudes for flows from each inclination during rigid bed case runs. The data, a summation of localized and averaged bed forces, focuses on the bed forces within an approximately 0.012 m length section on the ramp surface over the duration of each flow. These regressions show a time lapse of bed

forces at one position on the substrate. The Eulerian temporal regressions reveal irregular distribution patterns of discrete bed force localizations for each incline in both time and magnitude. Visual inspection of the progressing experimental flows also exposed dynamic irregular spatial force localization distribution patterns.

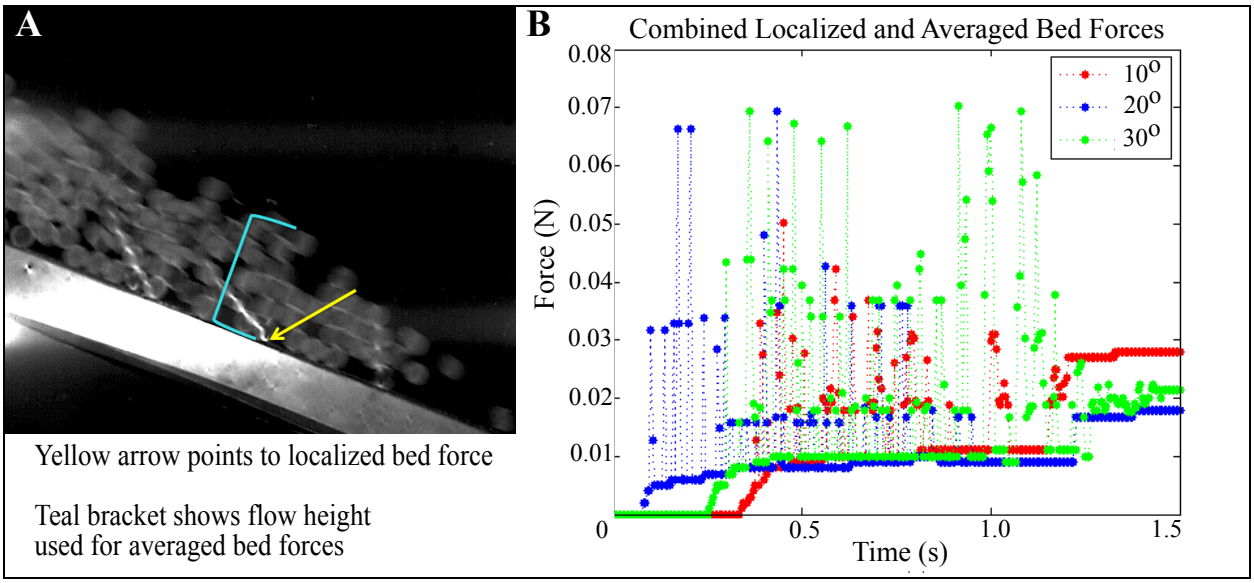

Figure 5. A. Sample image illustrated to show where localized and averaged forces are derived. B. Eulerian temporal regressions describe cumulative bed force magnitudes due to force chains combined with the flow body for each inclination during rigid case runs.

Several still frame images from the recordings of each incline – bed pairing, 43 total, were selected to evaluate localized versus averaged bed forces (Figure 6); and to determine the correlations between bed force directional components with chain inclinations relative to the substrate and total bed force magnitudes. Criterion for the image selections were clarity of force chains, fringe patterns and disk morphologies, as well as visibility of the granular flow surface in measurable proximity to the substrate. Mean local (force chain) bed force relative to mean average (from flow height) bed force magnitude was 435.62 ± 0.59 % for rigid bed conditions and 738.32 ± 0.57 % for erodible bed conditions. Taken from 29 rigid case and 14 erodible case

images, these values include results from both focus areas of the experiments. The mean local bed force was obtained from analyzing the fringe factor of the chain member contacting the substrate, and the mean average bed force was calculated from the height of the flow normal to the force chain – substrate contact point.

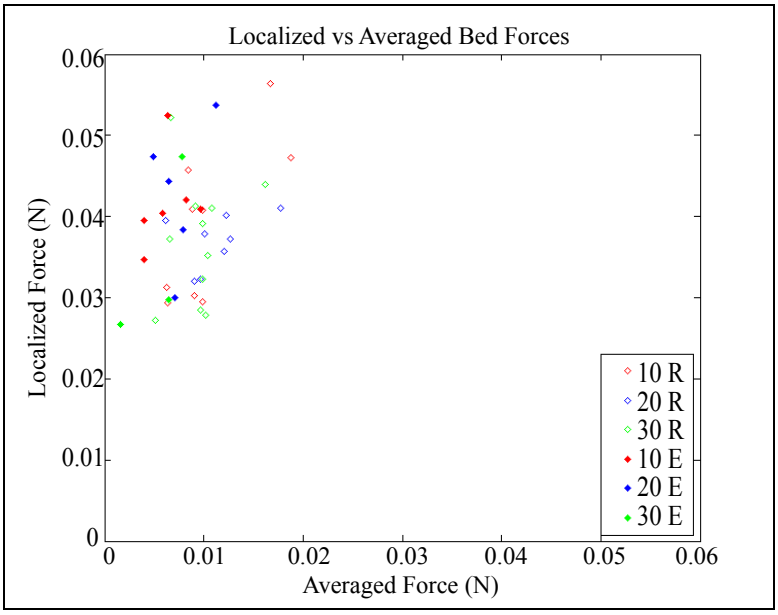

Figure 6. Localized bed force magnitudes from force chains compared to averaged bed force magnitudes calculated from flow body height for rigid and erodible cases.

Using the Pearson product-moment method, no significant correlation was found between bed force directional components and chain inclinations. Although no strong correlations were discovered, the bed force directional components and total bed force magnitudes showed small positive correlations; while the normal versus shear components displayed a medium negatively correlated relationship.

Because photoelastic material was utilized to occupy the erodible bed section, our experiments provided an avenue to investigate bed force propagation into the substrate. Employing the same techniques used to determine bed forces at the flow – substrate contact

point, we recorded the extent of optical activity observed in the cutout bed section resulting from flow contact with the substrate. Propagation extent versus bed force magnitude is plotted in Figure 7. Note that propagation was limited by edge effects of the section domain so that the represented values are minimal; and that 30-degree information is limited due to corrupted data. The data for the bed force propagation shows no significant correlation between applied force and propagation extent, as the correlation coefficient of 0.328 is much lower than the 0.532 minimum value required for significance at the 95% confidence level at the given sample size. As observed in Figure 8, we find evidence of optical activity in the substrate ahead of the flow front due to forces applied upslope by the flow.

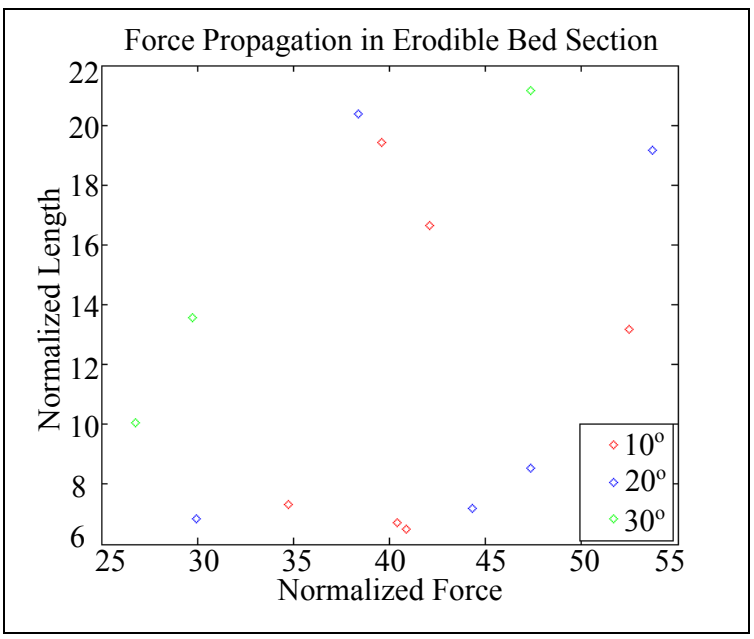

Figure 7. Extent of force propagation into erodible bed section correlated to magnitude of bed force at chain-bed contact point for each ramp inclination. Length scale is normalized by the diameter of a particle, and force is normalized by the force of one particle's gravitational acceleration.

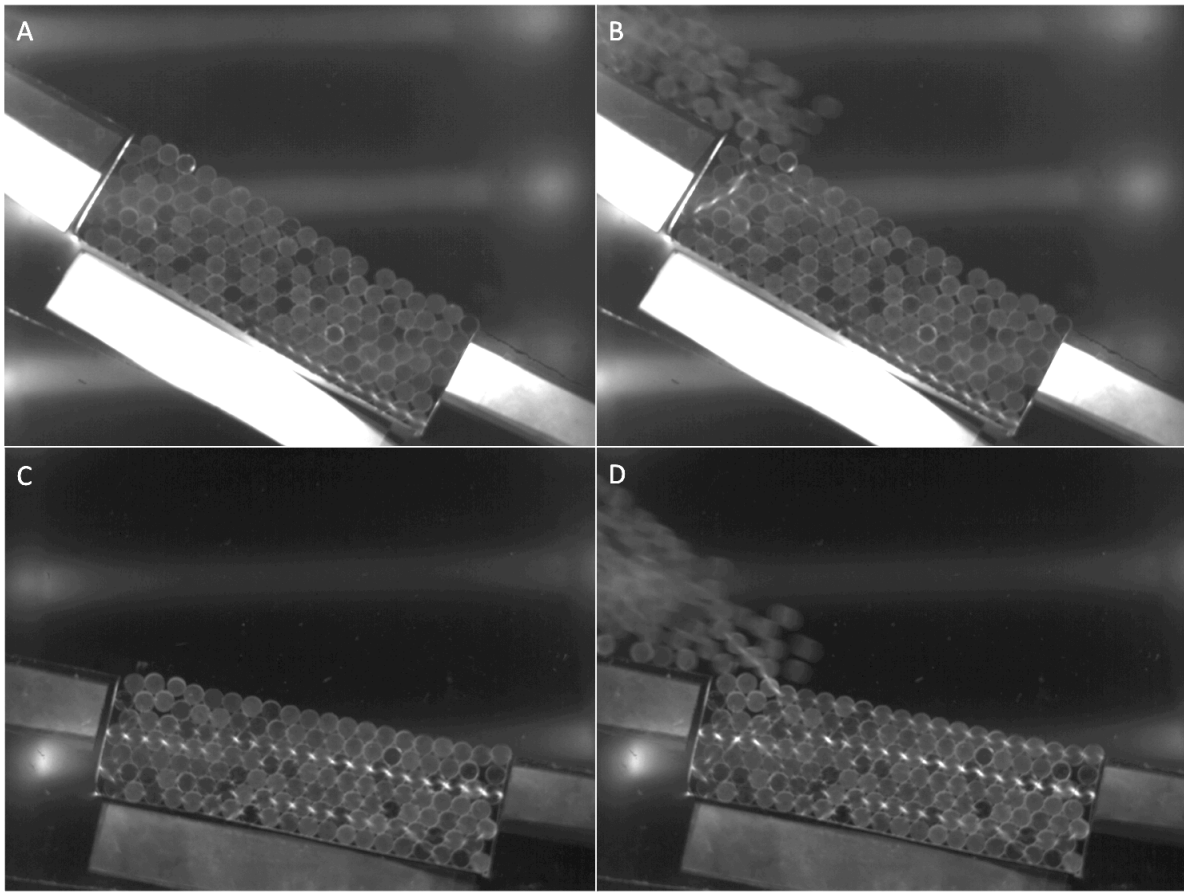

Figure 8. Pictured above are images of the erodible bed section, which show force propagation into the bed section and ahead of the flow front. The top two pictures (A, B) are the 30 degree case, and the bottom two pictures (C, D) are the 10 degree case. The left column (A, C) shows the bed sections before the flow impacted them, and the right column (B, D) shows the flows contacting the erodible bed sections.

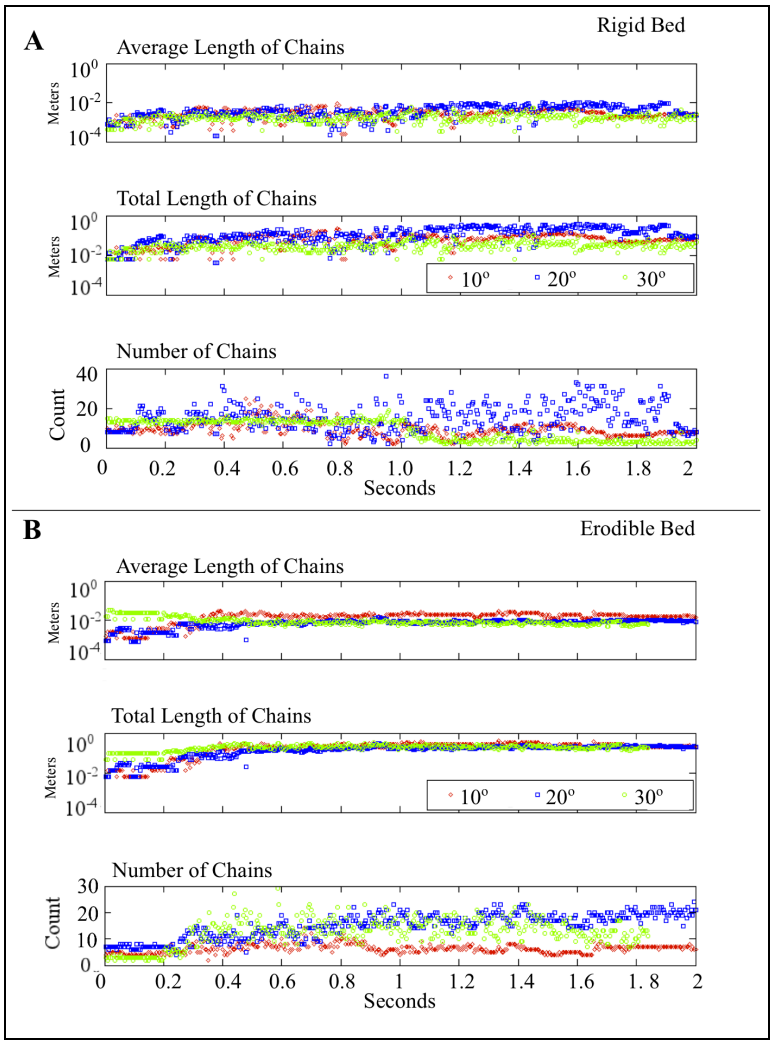

Figure 9. A. Temporal regressions average length, total length, and number of force chains for each incline from rigid bed experiments. B. Temporal regressions average length, total length, and number of force chains for each incline from erodible bed experiments.

Figure 9A and B presents temporal regressions showing 2 second durations of average length, total length, and number of force chains for each incline from rigid bed and erodible bed experiments, respectively. Because the area captured by the camera frame was limited, the data displayed in the regressions is representative of a fraction of the flow body. The rigid bed regression images were recorded at the upslope focus area, which centered on the release gate. The erodible regression images were recorded at the down slope focus area, which centered on the cutout bed section. Analysis of the chain length and number regressions showed no patterns.

CHAPTER 4. DISCUSSION

Once slope failure has initiated we are concerned with how the motion of the mass-wasting event evolves in time and space. A common approach to treat such inquiries utilizes mixture theory (Zanuttigh and Lamerti, 2007; Eringen, 2004; Pudasaini et al, 2005). The motion of a mixture is governed by equations of balance laws for mass, momentum and energy for its constituents (Atkin and Craine, 1976). Continuum theories utilizing this approach have proven useful for geophysical flows, especially depth-averaged models such as the Savage-Hunter (SH) model (Iverson, 1997; Denlinger and Iverson, 2004). The SH continuum model uses five assumptions: (i) flow body incompressibility, (ii) shallowness of flow body and small topographic curvature, (iii) Coulomb-type sliding, (iv) Mohr-Coulomb frictional behavior, and (v) approximately uniform velocity profiles within flows (Hutter, 2005). The SH model as typically applied does however have important limitations, typically neglecting entrainment and difficulty accommodating highly irregular flow paths (Iverson, 1997) – which are both practically relevant for natural flows. The SH-based computational model of Denlinger and Iverson (2004) effectively treats the irregular terrain issues with a hybrid finite volume/finite element procedure. Finite element bricks are employed to calculate the Coulomb stresses within the granular flow for this model. Because individual grains are not tracked, however, this model cannot treat force chain effects.

Erosion and/or entrainment of soils and bed sediments by fluid flow have been studied extensively (e.g. Garcia and Parker, 1991; Ancey et al, 2008; Sarmiento and Falcon, 2006). The erodibility of a given material can be influenced by several factors including, but not limited to the material type and amount, pore and eroding fluid compositions, grain geometry, and dynamic

conditions. Critical shear stress, usually denoted by τ_c, is often employed as the measure of erosion resistance (e.g. Arulanandan and Perry, 1983, Ancey et al, 2008; Sarmiento and Falcon, 2006). The critical shear stress designation typically denotes either: (i) a stress at which erosion initiates, or (ii) a stress that causes a particular erosion rate (Garcia and Parker, 1991; Ancey et al, 2008; Sarmiento and Falcon, 2006). Thus, sediments experiencing shear stresses below the critical shear stress would not erode and entrain while those experiencing shear stresses exceeding the critical value would erode and entrain into the flow. Entrainment functions, derived by combining critical shear stress criterion with bed-form descriptions and fluid mechanics, predict sediment entrainment rates (Garcia and Parker, 1991; Zanuttigh and Lamerti, 2007; Pudasaini et al, 2005; Iverson, 1997; Eringen, 2004).

Our experiments provide clear evidence of extreme localized bed forces relative to average bed forces. This work highlights that force chains, even in modest flows, can produce anomalous local bed forces that may exceed critical shear thresholds and initiate erosion and entrainment in granular systems which classical analysis would not recognize. Traditional continuum models that derive bed force values do not address the contributions of force chains to the flow substrate, and thus ignore any localization of bed forces due to such processes. Interestingly, the shear components of the bed forces derived from force chains carry the same order of magnitude as the normal bed force components for the chain inclinations observed. This further supports the assertion that force chains in granular flows may provide the 'plucking' shearing mechanism necessary to initiate erosion and entrainment. This is not to say, however, that force chain dynamics are the only mechanism contributing to substrate erosion and entrainment in geophysical flows.

Our experiments indicate significant propagation of bed forces into the flow substrate,

which are also results of dynamic force chain processes. Although limited due to edge effects of the experimental apparatus domain, our data suggests that bed forces applied during force chain contact with the bed can propagate on the same length scales as force chains within the flow body. For force chains contacting the bed near the head of the flow, this means that the bed forces may propagate ahead of the flow front, affecting the substrate particles before the flow body reaches their proximity. As force chains can cause significant perturbations to the stresses at the bed, this work suggests that sub-grid models may be necessary when applying continuum models to granular flow erosion problems. Further, our results imply that discrete-element computations are necessary to treat force chain processes in geophysical flows.

While our work has focused on dry granular flows, the debris flow work of Iverson (1997) and Iverson et. al. (2011) carries significant implications that are applicable to our results. Debris flows, approximately equal parts solid and fluid, are a specialized case for the granular flow regime. Iverson's large-scale flume experiments (1997) reveal that measured stresses at the base of debris flows change rapidly – which is interpreted as an indication that groups of grains or individual grains and adjacent fluid have a dynamic interaction with the flow boundary. In recent work, Iverson et. al. (2011) observed that shear deformation of the bed coincided with increased local pore fluid pressures; and these latest experiments also exhibit rapid fluctuations in measured pore pressures and normal traction that the flow base. Pressure transmission via interconnected pore water in flows with sufficient saturation also appears to be an important mechanism in the frictional reduction in debris flows that results in extended run-out distances. These findings are not, however, inconsistent with the notion of force localizations at the flow bed via granular force chains. A relationship between localizations of bed forces via granular processes and pore pressure fluctuations has not been established, however speculation warrants

further investigation.

The dual-state nature of debris flow constituents behave such that stand-alone continuum or discrete-element simulations are incapable of treating the physics involved in the entirety of the flow. As such, simulations that treat the carrier fluid (or gas) phase as continua and the dispersed solid phase as discrete particles – referred to as continuum discrete method (CDM) simulations – provide an avenue to encompass the physics required for these multiphase geophysical flows. Several code options are available for CDM simulations, such as commercially available Fluent and Barracuda and open sources codes like MFIX-DEM and OpenFoam (Kashiwa and Rauenzahn, 1994). Each of these CDM codes solve similar types of governing equations for the carrier phase, but may have different approaches the dispersed phased. For instance, OpenFoam utilizes parcel-based tracking; in which a finite number of parcels that can represent a fractional or real number of particles are tracked. MFIX-DEM, on the other hand, represents the dispersed phase as actual individual particles and directly resolves the collisions based on the soft-sphere approach (Cundall and Strack, 1978). CDM simulations employing particle tracking are generally limited to small problem sizes, however, due to the high computational cost of the particle neighbor searching algorithms (Garg et. al., 2010).

Dufek and Bergantz (2007) successfully adapted the MFIX multiphase code for simulations investigating pyroclastic flows with unique saltating and leaky boundary conditions. In contrast to debris flows, a hot gaseous carrier phase rather than a fluid dominates the pyroclastic flows considered. Particle-bed interactions for the saltating boundary condition cause increased bed-load, extended particle residence times within the flow body, and particle entrainment; which result in greater run-out distances. The leaky boundary condition (i.e. the flow traverses water) causes inhibition of bed-load formation, which dilutes the particle volume

fraction in the flow and results in buoyancy reversal and entrainment of ambient fluid – terminating any further propagation as a ground-hugging current. Although force chain contributions were not considered in these pyroclastic simulations, the results of the saltating boundary condition runs may harbor force chain effects. The shear required for particle entrainment at the flow base may operate partly through the mechanism of force chain dynamics. Because of the several points of grain contacts required for force chains to evolve, pyroclastic flow particle volume fractions may be too small to accommodate frequent force chain activity. Therefore, statistical inferences concerning variations of particle volume fractions within pyroclastic flow bodies are needed to determine if force chain mechanisms are actually relevant in these processes.

In the context of the chain conservation and force balance formulations of Furbish et. al. (2008) (equations 1 & 2), we find that experiments of our type may provide useful information for constraining some of the key factors in the theoretical construct. The force balance in equation 2 describes the force F associated with force chains over an area B. If we assume B is stationary with respect to time, then we can extract force information from sequential frames of our experimental runs and apply it to the force balance in equation 2. Summing the forces on each force chain member in B, measured from the fringe factor, gives F. The abundance of chain length data provided by photoelastic experimentation and analysis combined with shear rate information may allow prescription of discrete values or ranges of values permissible for α. Given as the reciprocal of mean free time (between collisions of free moving grains), a value of ε may be obtainable from image analysis of sequentially parsed frames taken from high-speed video recording of the experimental flows. While the information acquired in this way would not be directly applicable to natural flows, it would certainly be useful to reach a comprehensive

understanding of how these parameters relate in empirical systems. This type of knowledge would help advance the capability of granular flow simulations.

4.1 Conclusions

Through utility of photoelastic inquiry, this study provides quantitative evidence of dynamic force chain activity in gravity driven granular flows; and reveals the significance force chain activity carries for conditions at the flow substrate. Our experiments provide a dataset to validate discrete element granular flow models both qualitatively and quantitatively. Inter-particle force and bed force data provide constraints on force magnitudes while the images reveal geometric information in both spatial and temporal domains. In the future, experiments of this type may increase scale sizes for the empirical systems; which would be especially useful for the erodible bed case. A larger erodible bed section may eliminate the observed edge effects and allow for more amorphous substrate particle arrangements. Polydiversity within the granular media and addition of fluids into the system would also strengthen experimental applicability to natural systems, which would benefit simulation models requiring the utility of quality empirical data. With validation from small-scale 2D systems, numerical models can expand their scope to more sophisticated large-scale 3D simulations. As empirical relevance to naturally occurring events becomes stronger, so shall the success of computational simulations relying on validation data.

REFERENCES

Ancey, C., Davison, A., and Bohm, T. (2008) Entrainment and motion of coarse particles in a shallow water stream down a steep slope: Journal of Fluid Mechanics. Vol. 595, pp. 83-114.

Arulanandan, K., and Perry, E. B. (1983) Erosion in Relation to Filter Design Critieria in Earth Dams: Journal of Geotechnical Engineering. Vol. 109, pp. 682-698.

Atkin, R. J., and Craine, R. E. (1976) Continuum Theories of Mixtures – Basic Theory and Historical Development: Quarterly Journal of Mechanics and Applied Mathematics. Vol. 29, pp. 209-244.

Behringer, R. P., et al. (2008) Why Do Granular Materials Stiffen with Shear Rate? Test of Novel Stress-Based Statistics: Physical Review Letters. Vol. 101, 268301.

Cundall, P. A., and Strack, O. D. L. (1978) The Distinct element Method as a Tool for Research in Granular Media: National Science Foundation Technical Report. NSF Grant ENG76-20711.

Denlinger, R.P., and Iverson, R. M. (2004) Granular avalanches across irregular three-dimensional terrain: 1. Theory and computation: Journal of Geophysical Research. Vol. 109, pp. 1-14.

Dufek, J., and Bergantz, G. W. (2007) Suspend load and bed-load transport of particle-laden gravity currents: the role of particle-bed interaction: Theoretical and Computational Fluid Dynamics. Vol. 21, pp. 119-145.

Eringen, A. C. (2004) A mixture theory for geophysical fluids: Nonlinear Processes in Geophysics. Vol. 11, pp. 75-82.

Garcia M., and Parker G. (1991) Entrainment of Bed Sediment into Suspension: Journal of Hydraulic Engineering. Vol. 117, pp. 414-435.

Garg, R., et. al. (2010) Documentation of open-source MFIX-DEM software for gas-solids flows: https://mfix.netl.doe.gov/documentation/dem_doc_2010.pdf.

Geng, J., et. al. (2003) Green's function measurements of force transmission in 2D granular materials: Physica D. Vol 182, pp. 274 – 303.

Furbish, D. J., et. al. (2008) Thermal and force-chain effects in an experimental, sloping granular shear flow: Earth Surface Process Landforms. Vol. 33, pp. 2108–2117.

Hutter, K., et. al. (2005) The Savage-Hunter avalanche model: how far can it be pushed?: Philosophical Transactions of the Royal Society A-Mathematical, Physical, and Engineering Sciences. Vol. 363, pp. 1507-1528.

Iverson, R. (1997) The Physics of Debris Flows: Reviews of Geophysics. Vol. 35, pp. 245-296.

Iverson, R., et. al. (2011) Positive Feedback and momentum growth during debris-flow entrainment of wet bed sediment: Nature Geoscience. Vol. 4, pp. 116-121.

Kashiwa, I., and Rauenzahn, R. M. (1994) A Multimaterial Formalism: Technical Report LA-UR-94-771 Los Alamos National Lab.

Majmudar, T. S., et. al.(2005) Contact force measurements and stress-induced anisotropy in granular materials: Nature. Vol. 435, pp. 1079-1082.

Majmudar, T. S., et. al.(2007) Jamming transition in granular systems: Physical Review Letters. Vol. 98. 058001-1 – 058001-4.

Mangeney, A., et. al. (2007) Avalanche mobility induced by the presence of an erodible bed and associated entrainment: Geophysical Research Letters. Vol. 34, L22401.

McDougall, S., and Hungr, O., (2005) Dynamic modeling of entrainment in rapid landslides: Canadian Geotechnical Journal. Vol. 42, pp. 1437 – 1448.

Muthuswamy, M., et. al. (2006) How do interparticle contact friction, packing density, and degree of polydispersity affect force propagation in particulate assemblies?: Journal of Statistical Mechanics: Theory and Experiment. P09003.

Pudasaini, S. P., et. al. (2005) Modelling debris flows down general channels: Natural Hazards and Earth System Sciences, Vol. 5, pp. 799-819.

Silbert, L. E., et. al. (2003) Granular flow down a rough inclined plane: Transition between thin and thick piles: Physics of Fluids. Vol. 15, pp. 1 – 10.

Vishay Precision Group (2010) Calibration of Low-Modulus PhotoStress Coatings: Application Note IB-238-1. Micro-Measurements: www.micro-measurments.com. Document No.: 11238, pp. 1 – 2.

Vishay Precision Group (2005) Introduction to Stress Analysis by the PhotoStress Method: Technical Note TN-702-2. Micro-Measurements: www.vishaymg.com. Document No.: 11212, pp. 1 – 14.

Zanuttigh, B., and Lamberti, A. (2007) Instability and surge development in debris flows: Reviews of Geophysics. Vol 45, pp. 1-45.